

Contents lists available at ScienceDirect

Petroleum Science

journal homepage: www.keaipublishing.com/en/journals/petroleum-science



Original Paper

Thermal characteristics and removal mechanism of high energy plasma jet rock-breaking



Yan-Cong Han, Chao Zheng **, Yong-Hong Liu *, Xin-Lei Wu, Ren-Peng Bian, Peng Liu

China University of Petroleum East China, Qingdao, 266580, Shandong, China

ARTICLE INFO

Article history: Received 8 April 2024 Received in revised form 18 December 2024 Accepted 18 December 2024 Available online 20 December 2024

Edited by Jia-Jia Fei

Keywords: Plasma jet Rock-breaking mechanism Thermal spalling Granite melting Rock-breaking efficiency

ABSTRACT

High-energy plasma jet rock-breaking technology is regarded as a very promising new drilling approach for deep hard rock, attributed to its high energy density, high rock-breaking efficiency, absence of mechanical wear, and capability to drill high-hardness rocks. However, the thermal characteristics and rockbreaking mechanism of plasma jet remains unclear. This study thoroughly investigates the internal temperature distribution characteristics of granite and the thermal removal mechanism of plasma jet with combined experimental and numerical approaches. The spallation temperature of granite is calculated based on the Weibull statistical theory of tensile failure. A numerical model of the thermal melting process of granite is developed to obtain the erosion morphology and temperature distribution characteristics during the rock-breaking process. The results indicate that the spallation temperature induced by the plasma jet is approximately 557 °C, and the experimentally obtained hole profile on the upper surface coincides with the isotherm corresponding to the spallation temperature from the simulation. The temperature gradients of granite in the radial and axial directions of plasma arc operation can reach up to 38.79 and 66.13 °C/mm, respectively. And the heat-affected region expands with increasing current. The optimal removal efficiency can be achieved between 20 and 30 s under various plasma current conditions, with the maximum value of 1188 mm³/s at a current of 300 A. The plasma jet rock-breaking process can be characterized into three stages: dominant spalling in the early rockbreaking stage, followed by the coexistence of hot melting and spalling in the middle stage, and dominant high-temperature melting removal in the later stage. The results of this study provide theoretical guidance for engineering application of high-energy plasma jet rock-breaking drilling.

© 2025 The Authors. Publishing services by Elsevier B.V. on behalf of KeAi Communications Co. Ltd. This is an open access article under the CC BY-NC-ND license (http://creativecommons.org/licenses/by-nc-nd/4.0/).

1. Introduction

As the development of conventional oilfield enters its later stages and the global shifts towards green energy, the focus is increasingly directed towards unconventional and clean energy sources, such as deep oil, shale gas, and geothermal energy etc. (Pink et al., 2023; Sambo et al., 2023). Currently, the globally proven recoverable unconventional oil and gas resources are estimated at 4.29×10^{11} tons and 2.27×10^{14} m³, respectively, with abundant reserves (Dai et al., 2014). Moreover, global terrestrial hot dry rock (HDR) energy, a form of geothermal energy, amounts to

approximately 4.95 trillion tons of standard coal, which is nearly 30 times the total global fossil energy reserves (Aghahosseini and Brever, 2020). However, these resources are mostly stored in ultradeep reservoirs characterized by high temperature and stress. Reservoir rocks are mainly composed of metamorphic and crystalline rocks, such as granite, posing significant drilling challenges due to their high strength, high tightness, and low permeability (Li et al., 2020; Jia et al., 2023). High geopathic stresses, high geothermal and other extremely complex conditions will lead to problems such as low drilling speed and severe drill bit wear when drilling deep hard rock by traditional mechanical drilling. The tool replacement time can exceed 30% of the construction time, and may even hinder the implementation of the project during the drilling process (Rossi et al., 2020; Baruffati and Ngueguim, 2023; Jing et al., 2024). Breaking through the technical bottleneck of deep hard rock drilling is the key to promoting the development of geothermal energy (Gao et al., 2022).

E-mail addresses: zhengchaovip@126.com (C. Zheng), liuyhupc@163.com (Y.-H. Liu).

^{*} Corresponding author.

^{**} Corresponding author.

To address the problem of mechanical bit wear and replacement during hard rock drilling, some new noncontact rock-breaking methods have been developed. These methods can be classified into three categories: impact rock-breaking, thermal stress rockbreaking and erosion wear rock-breaking. High-pressure water jet rock-breaking primarily occurs through impact pressure and the water wedge effect, which are combined with breaking and cooling lubrication to enhance rock-breaking efficiency (Li et al., 2017). However, when breaking hard rock, extremely high water pressure (>200 MPa) is required, and the energy consumption is 40-70 times higher than that of mechanical rock-breaking (Wang et al., 2023). Particle impact rock-breaking is caused by erosion and wear, through high-speed particle impact on the rock, resulting in impact stress wave breaking, low energy consumption and high efficiency. However, the existence of underground rock confining pressure inhibits fracture expansion and reduces the effectiveness of rock-breaking (Fang et al., 2022). Laser rock-breaking, microwave rock-breaking and flame jet rock-breaking induce local thermal stress in the affected region of the rock and reduce its strength (Bai et al., 2022). Rock-breaking by thermal stress has the advantage of concentrated energy input and avoids the serious wear problem of traditional drilling tools. But each method has some limitations and has not yet been applied in engineering. Laser energy attenuation in transmission is serious, rock-breaking energy consumption is high and it is not suitable for mining environment with high dust (Guo et al., 2022). The microwave generator is complex, and the effect varies significantly when breaking rocks of different compositions. So it is necessary to determine the wavelength and frequency according to the composition of the rock (Wei et al., 2019). Flame iet uses air combustion flame to break the rock, but the heat carried by air is limited and the density is low. Rock is mainly removed by heat spalling, resulting in lower rock-breaking efficiency (Wang et al., 2024a). The high-energy plasma rock-breaking technology in this study has high rock-breaking efficiency and low energy consumption by directly impacting and melting the rock through the highenergy-density plasma jet, so that the rock undergoes thermal spalling and melting removal. During operation, thermal energy is used for rock removal without macro drilling force and mechanical friction loss, therefore, a complex ground rotary power system is not required. Plasma drill bit can operate in both gaseous and liquid environments. A circle of air nozzles designed around the plasma drill bit forms an air barrier that isolates the plasma jet from the surrounding liquid environment (Sun et al., 2023). The fracturecreating effect of plasma arc can significantly increase permeability and weaken rock strength (Bazargan et al., 2017). Han et al. (2024) experimentally found that the plasma jet is more likely to cause the overall fragmentation of the rock sample. Sun et al. (2023) systematically investigated the influence of plasma parameters and confining pressure on the efficiency and specific energy of rock-breaking, and the results showed that plasma jets can achieve efficient removal regardless of whether hard or soft rock is broken. Moreover, under confining pressure conditions, the morphology of the crushing pit changes significantly, the efficiency is greatly improved, and the specific energy is approximately 0.5 times that under no confining pressure conditions.

Although plasma jets, flame jets, and lasers use high-temperature media to remove rocks, the rock-breaking process with plasma jets is complex. This process is characterized by spalling induced by thermal stress and melting caused by thermal energy. To understand the mechanism of plasma jet rock breaking, it is essential to examine the phenomena of heat spalling and melting separately. The plasma jet exerts very high heat flux on the rock surface to generate thermal stresses. The process in which thermal stress induces the expansion of rock cracks, forcing disc-shaped rock cuttings to eject violently from the surface is called thermal

spallation. The critical condition that induces thermal spallation of rock is the spallation temperature. Early studies established a foundation for understanding the thermal spalling mechanism, focusing on the process of spalling formation, heat transfer, and determining the spalling temperature through model development (Weibull, 1951; Tester et al., 1994). Rauenzahn and Tester (1989) employed Weibull's brittle failure statistical theory to explore the relationship between chip spalling and rock heterogeneity. Kant et al. (2016) determined the minimum boundary conditions required for rock chip spalling under hydrothermal injection conditions by using rock surface temperatures and heat transfer coefficients. The thermal melting removal method has primarily been studied through experimental analyses. Researchers such as Li and Rui used the finite element software ANSYS to simulate the thermal melting process, but the surface heat source applied in the simulation had limitations. It failed to accurately reflect the depth-wise loading of the heat source (Li et al., 2018; Rui and Zhao, 2021).

In summary, high-energy plasma jet rock-breaking is an innovative and highly efficient technology. The breaking process involves different interacting removal methods. There is a lack of coupled research on different thermal removal methods in the existing literature. Therefore, it is necessary to study the rockbreaking process of plasma jet systematically to elucidate its mechanism. In this study, the temperature rise characteristics of granite during rock-breaking are studied, the spalling temperature is estimated based on Weibull statistical theory, and a numerical simulation of thermally melted granite is performed. A systematic analysis is conducted to compare the experimental results by integrating the spalling and melting processes. This study aims to reveal the mechanism of plasma jet rock-breaking, examine the thermal effects of plasma jets, and provide a theoretical foundation for engineering applications of plasma jet rock-breaking technology.

2. Experimental studies

2.1. Experimental apparatus and procedures

Fig. 1(a) shows the self-developed high-energy plasma jet rockbreaking rig with temperature measurement experimental system. The temperature of granite during plasma jet rock-breaking at atmospheric pressure was measured. The high-energy plasma power supply can provide direct current ranging from 30 to 350 A. The positive and negative poles are connected to the anode and cathode of the plasma drill bit, respectively, forming a closed circuit. Fig. 1(b) illustrates a schematic diagram of the plasma drill bit with an outer diameter of 40 mm and an anode nozzle aperture of 10 mm. The compressed air is adjusted and stabilized using the flow valve and electromagnetic flow meter before being channeled into the plasma torch electrode chamber, serving as the medium for generating arc plasma. The cooling system utilizes a water tank equipped with a circulating pump to cool the plasma drill bit. The plasma drill bit is clamped by a height-adjustable experimental bench, aligning the geometric center of the granite with the axis of the plasma drill bit. The distance between the granite surface and the terminal face of the plasma drill bit is maintained at 40 mm. Precision armored K-type thermocouples (WRNK-191, China, 3 mm \times 100 mm) are inserted into the prepared holes of the rock sample. The temperature signals are transmitted through the thermocouple wire (OMEGA, USA, temperature measurement range -40-1200 °C, accuracy ± 0.5 °C) to the temperature recorder (JK350, China, 0.01–200 Hz), with the data subsequently stored on the computer.

To ensure stable temperature data acquisition, the temperature logger is activated 30 min prior to the experiment for

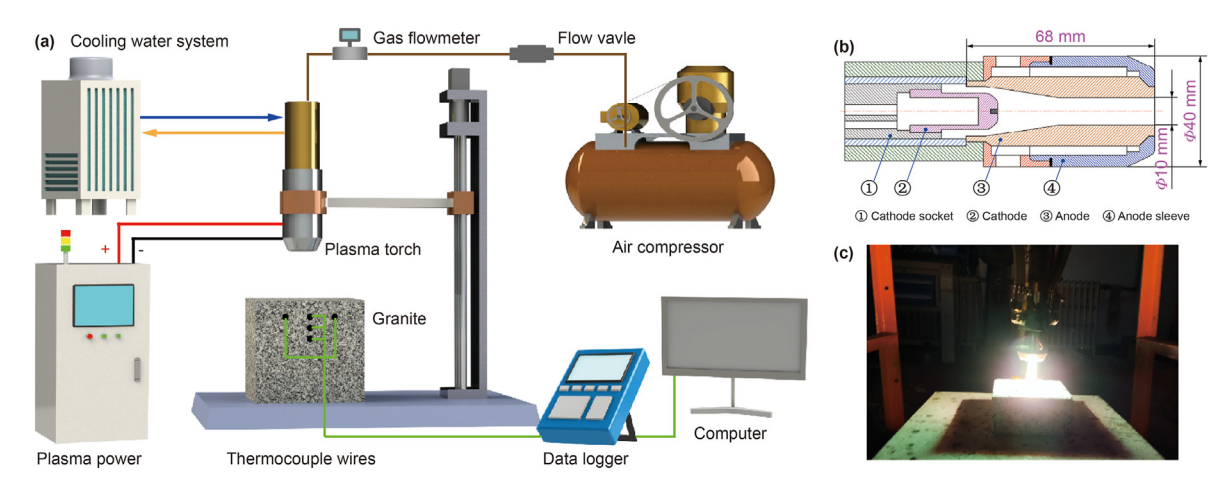


Fig. 1. Plasma jet rock-breaking experimental rig (a), plasma torch schematic (b), and photograph of the rock-breaking process (c).

acclimatization to room temperature, and the acquisition frequency is set at 10 Hz. Then, the plasma power supply, air supply system, and water-cooling system are activated. The plasma current is configured, the compressed air gas flow rate is adjusted to 40 L/ min, and the water circulation system is subsequently inspected. The arc ignition is activated and maintained for 30 s. Subsequently. the temperature logger continues to record data for an additional 10 s for accuracy. After the granite cooled to room temperature, the hole radius and depth were measured using digital vernier calipers. and the rock samples were weighed using electronic scales. The drilling depth per unit time is defined as the rate of penetration (ROP), the amount of rock removed per unit time is the removal efficiency, and the energy output from the plasma power supply required to remove unit mass of rock is the specific energy (SE). The plasma output energy is measured by an electrical energy sensor. Fig. 1(c) presents a photograph captured during the rock-breaking process.

2.2. Experimental sample

At present, the hot dry rock reservoirs developed by enhanced geothermal systems are almost entirely composed of granite, with depths ranging from 1.9 to 4.4 km and temperatures from 150 to 200 °C. They are characterized by high temperature, high stress, and low permeability (Li et al., 2020; Zhu et al., 2023; Wang et al., 2024b). In this study, the granite collected in Rizhao, China was selected as the research object. The thermodynamic parameters of rock samples were tested, and the results are shown in Table 1. The test results show that the rock sample has a drillability level of 9–10, a compressive strength of 165 MPa (a confining pressure of 20 MPa), and is almost seamless, making it suitable as research object. The sample dimensions were set at 100 mm \times 100 mm \times 100 mm. Five

Table 1 Thermodynamic parameters of granite.

Parameter	Symbol	Value	Unit
Density	ρ	2.68×10^3	kg/m ³
Young's modulus	Е	5.295×10^{4}	MPa
Axial strength	σ_0	77	MPa
Compressive strength	$\sigma_{ m b}$	165	MPa
Poisson's ratio	υ	0.233	_
Drillability level	$K_{\rm d}$	9-10	_
Specific heat capacity	$C_{\rm p}$	960	J/(m ³ ·°C)
Thermal conductivity	ĸ	2.84	W/(m·°C)
Coefficient of thermal expansion	β	7.8×10^{-6}	1/°C

holes was drilled on the rock sample with configurations illustrated in Fig. 2(a) and (b). The test points along the radial direction of the plasma arc operation were designated as R1, C1, and R2, and the three test points along the axial direction of the plasma arc were labeled as C1, A1, and A2. The experimental comparison reveals that the presence of the temperature measuring hole has almost no effect on the rock-breaking effect under the action of plasma jet. Therefore, the influence of drilling on the strength of the rock sample during the rock sample preparation process can be ignored. The mineral compositions of the granite samples were analyzed for their using an X-ray diffractometer (PANalytical X'Pert3 Powder, Netherlands), with the findings presented in Fig. 2(c). The physical properties of the rock samples used in this study were tested and the results are shown in Table 1.

2.3. Experimental results analysis

At the C1 hole, the temperature variation of granite under five different plasma current conditions was monitored, with the results depicted in Fig. 3(a). The plasma jet started to break the rock at 10 s and end at 40 s. As the plasma current increases, the rate of temperature increase in the granite accelerates, resulting in higher final temperature values. Given the high specific heat capacity of granite, the temperature of granite begins to change only after 10 s from the beginning of rock-breaking. Furthermore, the higher the plasma current, the earlier the temperature change occurs. Fig. 3(b) shows the final temperatures measured at the five test points with plasma currents of 100 and 300 A. The C1 point, located nearest to the center of the plasma arc, has the highest temperature. The temperature decreases in the axial direction away from the rock surface. Radially, the temperature is approximately symmetrical along the central axis. Notably, R1 and A1 are equidistant from C1, each at 20 mm. However, the temperatures at R1 and R2 are higher than that at A1, which indicates that the temperature gradient in the radial direction is smaller than that in the axial direction.

The rock chips generated during the rock-breaking process were collected, as shown in Fig. 4(a). This process yields three main types of rock chips: disk-shaped fragments, powdered particles, and vitreous enamel solidified from molten magma. The varied rock chip morphologies reflect distinct removal mechanisms. Two hundred manipulable rock chips were screened from the disk-shaped fragments, and statistical analysis was initiated. The maximum length (L), maximum width (W) (as shown in the schematic of a single rock chip in Fig. 4(a)), and thickness (H) of the rock chips were measured. The equivalent diameters (D_e) , calculated as

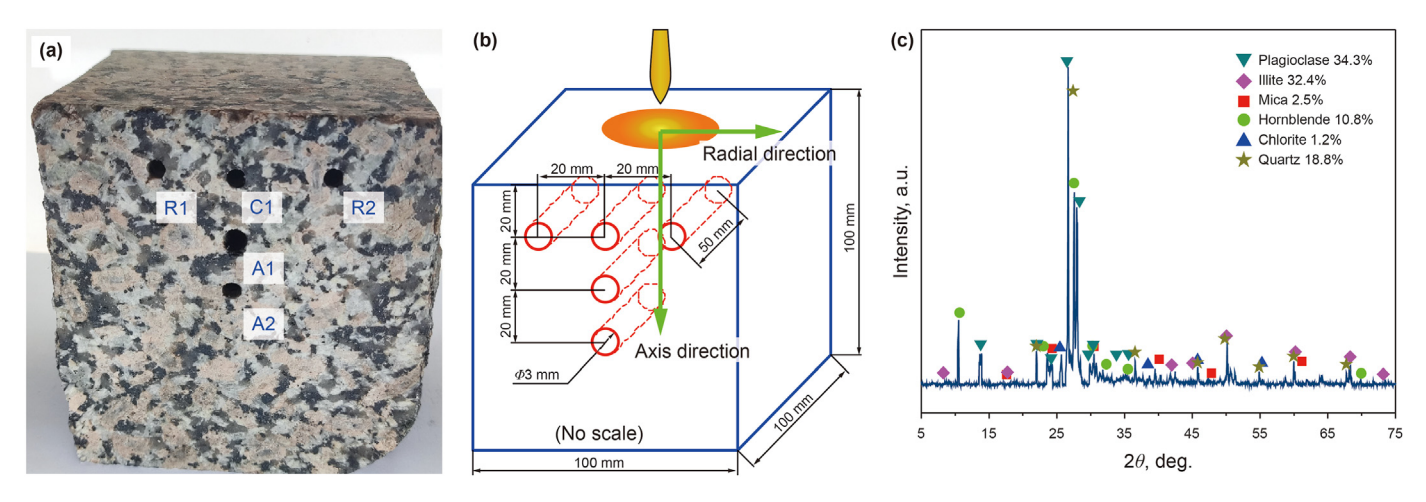


Fig. 2. Rock sample: (a) granite photo, (b) model schematic, (c) X-ray result.

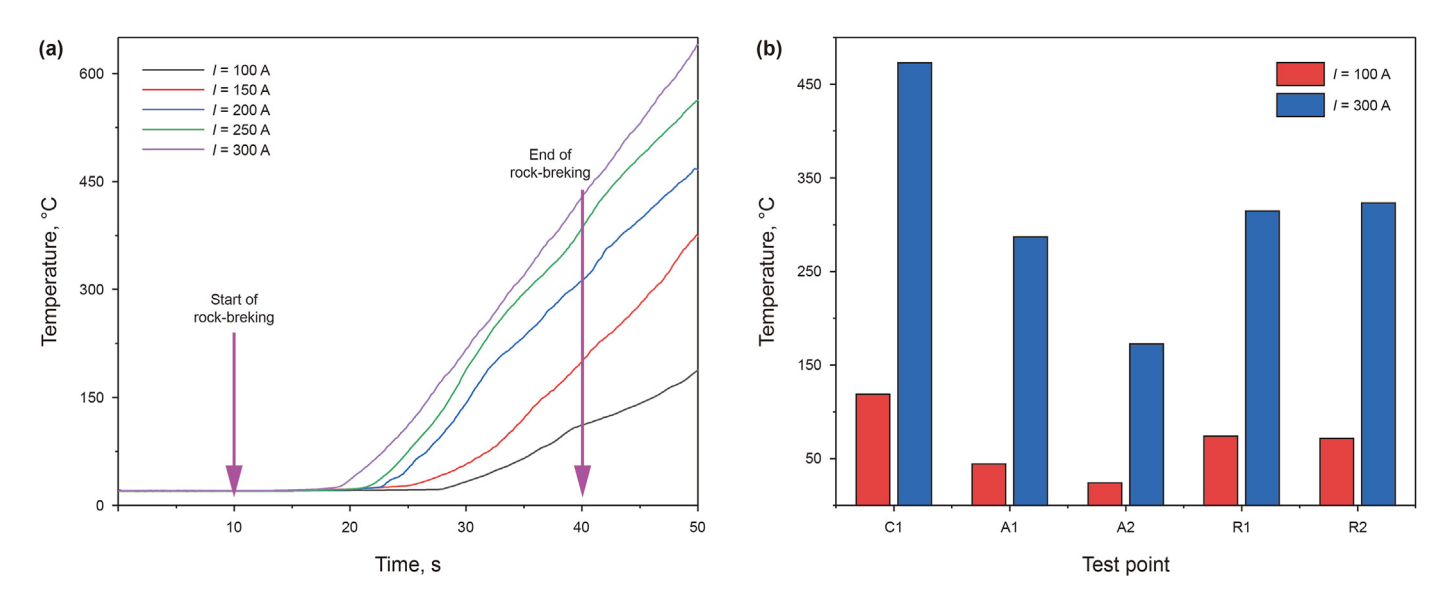
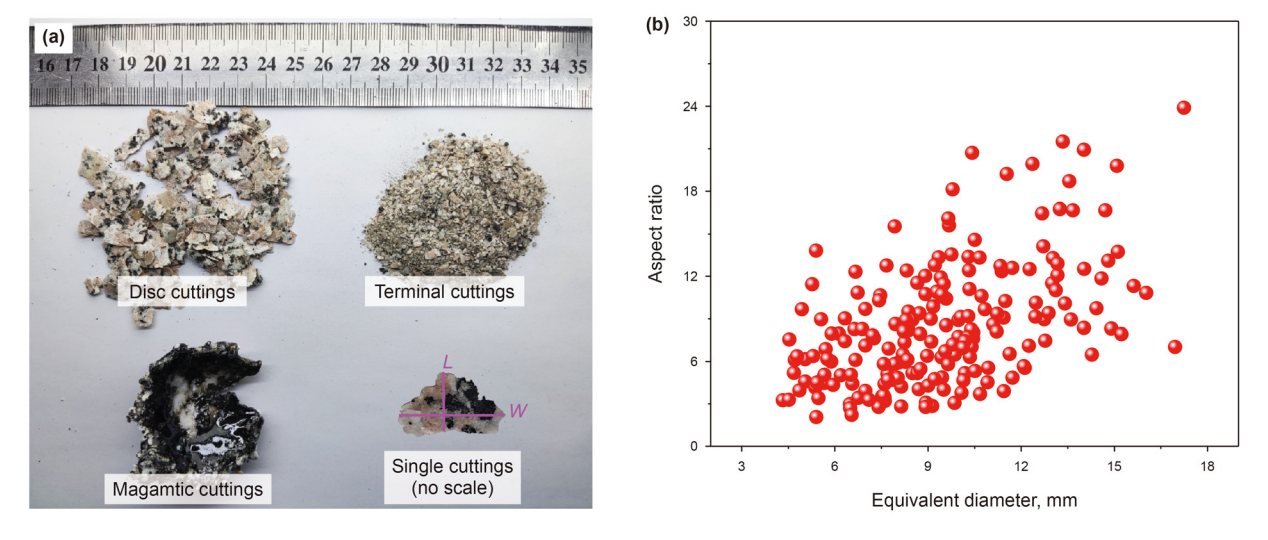


Fig. 3. Granite temperature: (a) at different plasma currents, (b) at different locations.



 $\textbf{Fig. 4.} \ \, \textbf{Rock chip photos (a)} \ \, \textbf{and characteristic statistics of disk rock chips (b)}.$

 $D_{\rm e}=2\cdot(L\cdot W/\pi)^{0.5}$, and the aspect ratio ($C_{\rm L}$), defined as $C_{\rm L}=D_{\rm e}/H$, were employed to describe the shape of the rock chips. Fig. 4(b) shows the statistical results, indicating that the aspect ratio ranging from 2.76 to 23.91, with average value of 8.53. These temperature and rock chip characteristic data will be utilized in Section 3 to calculate the spallation temperature and validate the accuracy of the plasma jet rock-breaking model.

3. Thermal effects of different removal methods for granite

3.1. Temperature conditions for the occurrence of thermal spalling

3.1.1. Theoretical model

Weibull proposed a statistical theory of failure that argued that inherent flaws within materials lead to both microscopic and macroscopic decomposition of laboratory samples (Weibull, 1951). The Weibull failure criterion has two main features: (1) it assumes the existence of defects within the material, yet disregards the quantity, size, and shape of the material, implying that the material properties and loading manner do not affect the results; (2) it employs a distribution of the failure strength derived from repeated testing rather than a single value. This is consistent with the hypothesis that tensile failure of brittle materials is based on macroscopic fractures caused by the most critical defects. Consequently, it is reasonable to use Weibull statistical theory model to describe thermal shock experiments. The spallation temperature of granite broken by a plasma jet is calculated by the following equation (Weibull, 1951):

$$G(\sigma) = 1 - \exp\left[-\int \left(\frac{\sigma}{\sigma_0}\right)^m dV\right] = 1 - \exp(-I)$$
 (1)

where G represents the cumulative probability of damage to the rock at stress levels below σ . m takes a value between 0 to ∞ , with a higher value indicating that the rock is more spatially homogeneous. When $m=\infty$, the material is perfectly homogeneous. σ denotes the applied load, and damage to the material occurs when $\sigma=\sigma_0$, which can be considered the rock strength per unit volume. Under median spalling conditions, the cumulative failure probability G takes the value of 0.5 (I=0.6390). If the relevant parameters are known, the spallation temperature can be predicted.

As the plasma jet acts on the surface of the granite, heat is transferred to the granite interior. The heat balance equation can be obtained using the following equation (Steen and Mazumder, 2010):

$$q = \frac{\kappa}{\alpha} \frac{\partial T}{\partial z} \nu_{ROP} - \kappa \frac{\partial^2 T}{\partial z^2}$$
 (2)

where T(z,t) is the temperature of the granite at distance z from the surface at time t, $^{\circ}$ C, obtained by the temperature sensor in Section 2.3; q is the heat flow density, W/m^2 ; v_{ROP} denotes the drilling speed, m/s; κ represents the thermal conductivity of granite, $W/(m\cdot^{\circ}C)$; α is the thermal diffusivity of granite ($\alpha=\kappa/(\rho C_p)$), m^2/s ; ρ is the density of granite, kg/m^3 ; C_p is the specific heat capacity, $J/kg\cdot^{\circ}C$. Given that the radial influence range of the plasma jet (about 60–100 mm) significantly exceeds the axial penetration range (rock chip thickness 0.39–3.2 mm), Eq. (2) can be simplified as a one-dimensional heat transfer equation (Steen and Mazumder, 2010):

$$T(z,t) = \frac{2q}{\kappa} \sqrt{\alpha t} \operatorname{ierfc} \frac{z}{2\sqrt{\alpha t}} = \frac{2(T_{s} - T_{0})\nu_{ROP}}{\sqrt{\alpha}} \sqrt{t} \operatorname{ierfc} \frac{z}{2\sqrt{\alpha t}}$$
(3)

where T_s is the spalling temperature, °C; T_0 is the initial

temperature of the granite, $^{\circ}$ C. ierfc(x) denotes to the residual complementary error function.

In the calculations, the temperature jump that occurs when rock chips are thrown from the matrix is ignored. Considering the flaked rock chips as regular geometrical shapes, the differential volume dV is converted into $\pi(C_L z/2)^2 dz$, where z represents the distance from the granite surface, correlating to the thickness of each disk-shaped chip (Walsh and Lomov, 2013). Integration of Eq. (1) under median spalling conditions, where $G(\sigma) = 0.5$, yields:

$$0.693 = \left(\frac{\sigma}{\sigma_0}\right)^m \frac{\pi C_L^2}{4} \int_0^\infty z^2 \exp\left(-\frac{m \nu_{ROP}}{\alpha}z\right) dz \tag{4}$$

Upon the incursion of a one-dimensional temperature wave into a rock mass, the compressive stress parallel to the surface is proportional to the temperature rise at that depth:

$$\sigma = \frac{\beta E(T - T_0)}{1 - \nu} \tag{5}$$

where β is the coefficient of thermal expansion, 1/°C; E is the Young's modulus of granite, MPa; and the dimensionless v denotes the Poisson's ratio of rock. The spallation temperature prediction equation can be obtained by substituting Eq. (5) into Eq. (4) and integrating:

$$T_{\rm s} = T_0 + \sigma_0 \left(\frac{1-\nu}{\beta E}\right) \left(\frac{m\nu_{ROP}\rho C_{\rm p}}{\kappa}\right)^{3/m} \left(\frac{2\times0.639}{\pi C_{\rm L}^2}\right)^{1/m} \tag{6}$$

3.1.2. Result analysis

The result shown in Fig. 5 is obtained by substituting the data from Section 2.3 into the equation in Section 3.1.1. As illustrated in Fig. 5(a), the spallation temperature increases with an increase in plasma current, and the increasing rate decelerates once the current exceeding 200 A. The overall temperature spans from 452.60 to 594.02 °C. This phenomenon can be attributed to the inherent characteristics of the plasma jet. As the plasma current increases, the plasma arc column elongates and intensifies, leading to a significant increase in the heat flux density, which instantaneously impacts the granite surface. The substantial temperature differential between the center of jet action and the surroundings causes the natural cracks in the granite to grow rapidly. Then, the rock breaks rapidly under the large currents. And the rock achieves a higher temperature compared to those with lower currents. Fig. 5(b) presents the spallation temperature deduced from temperature data obtained at the five test points under conditions of high current (300 A) and low current (100 A). Compared to A1, the spallation temperature at A2 diverges more significantly from that at C1, which may be due to the greater distance of A2 from the granite surface, the limited thermal diffusivity of the granite, and possible error in temperature measurement. The elevated temperature at R1 and R2, compared to A1, can be attributed to their location within the heat-affected region of the loose arc tail of the plasma jet rather than the direct impact zone at the center of the arc column with larger energy density. Consequently, the plasma jet exerts a diminished impact on these regions, necessitating higher temperatures to initiate dispersion. The average thermal spalling temperature value is about 557 °C. Additionally, the heat flow density for each operating condition has been calculated and is utilized in Section 3.1.3 for comparison with corresponding data from the literature.

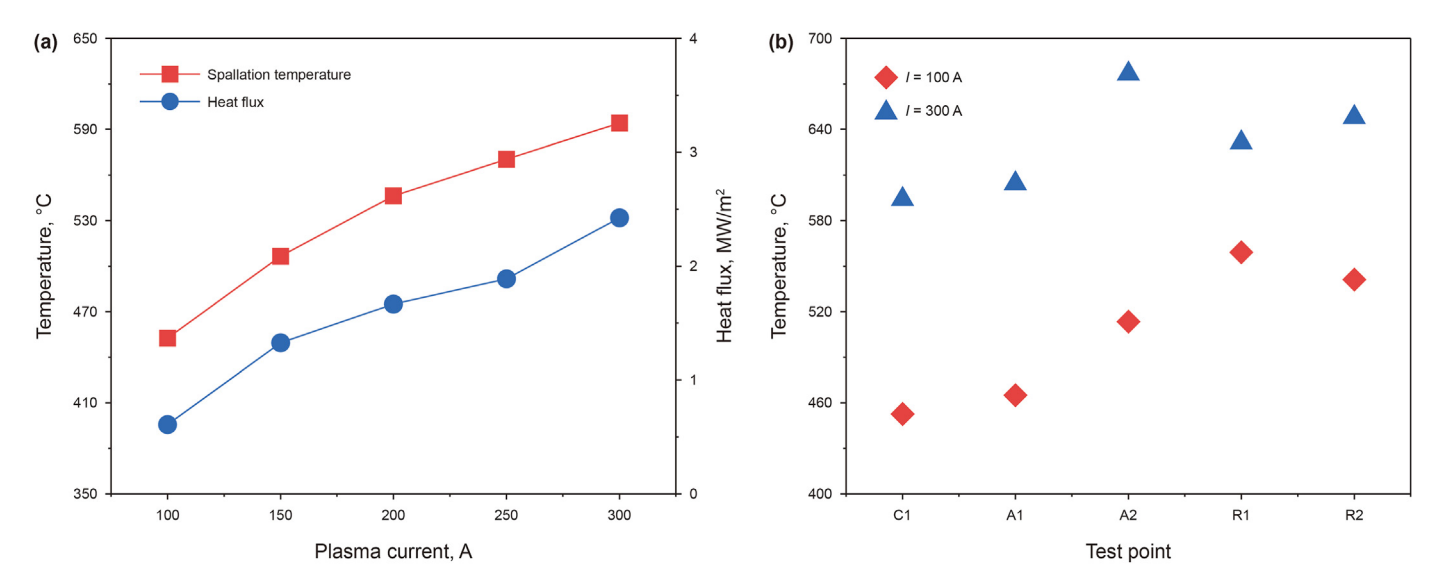


Fig. 5. Thermal spalling temperature: (a) different plasma current, (b) different test point.

3.1.3. Comparison and verification of plasma jet spalling temperature with other rock-breaking methods

To verify the reliability of the spallation temperature derived in this study, the results are compared with data from literatures (Rauenzahn and Tester, 1989; Wilkinson and Tester, 1993; Kant et al., 2016; Beentjes et al., 2019). Fig. 6 shows the spallation temperatures of plasma jets and other rock-breaking methods, presenting a consistent trend. This congruence substantiates the validity of the spallation temperature derivation for plasma jet rock breaking, thereby confirming its reasonableness and reliability.

The spallation temperature obtained in this study exhibits an approximately linear relationship with heat flux density, and the values are generally lower than those reported for flame and laser spallation methods in the literature. At similar spallation temperatures, plasma jets require a lower heat flow density than both flames and lasers to break rock. The variation in spallation temperatures across different rock-breaking methods can be attributed to two primary factors. Firstly, the discrepancy in granite types between this study and those cited in the literature, along with variations in physical property parameters, contributes to the observed differences in spallation temperatures. Secondly,

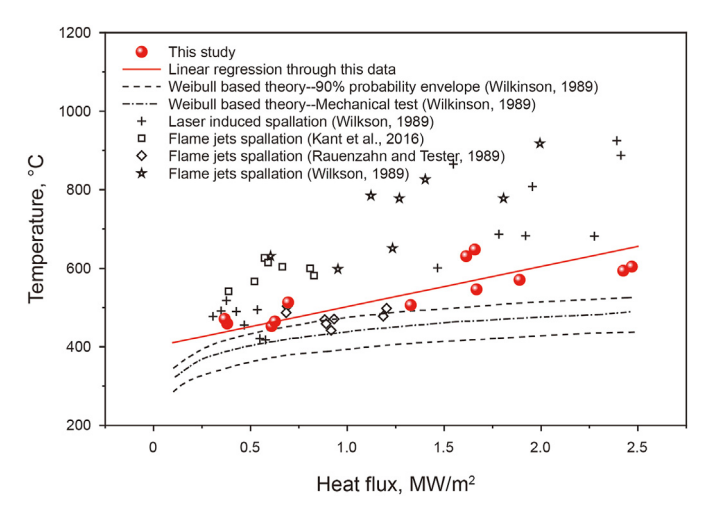


Fig. 6. Comparison of data from this study with published data of differeft rock-breaking methods (Kant et al., 2016; Rauenzahn and Tester, 1989; Wilkinson, 1989).

although both methods employ high-temperature media to interact with the rock surface, the distinct characteristics of arc plasma set it apart from flames and lasers. The temperature at the exit of the plasma torch can reach 10,000 °C, and the energy density can reach 10^3 MW/m². The temperature gradient from the core to the periphery of the plasma arc is significant. The gas medium exerts a substantial expansion force within the body torch. The gas is further compressed as it passes through the nozzle outlet. This compression forces the charged particles to be expelled from the nozzle at high velocities, generating a significant impact force. At this point, the jet velocity can reach the speed of sound (300 m/s) (Sun et al., 2020; Liu et al., 2023). The combination of these properties interacting on the rock surface leads to differences in breaking effectiveness.

3.2. Numerical simulation of the thermal melting process of plasma jet rock breaking

3.2.1. Finite element modeling

Plasma jet rock-breaking employs a high-temperature medium for thermally removing rock. It is meaningful to study the temperature field within granite. In this study, the finite element software COMSOL Multiphysics (version 6.2) is utilized to numerically simulate the plasma jet rock-breaking process. Fig. 7(a) shows a photograph of a plasma jet, where regions of higher brightness correspond to areas of increased energy density. Considering the characteristics of the plasma arc, a Gaussian cone heat source is selected. A rotating body heat source whose radius decreases with depth has a peak heat flow density that does not decay in the depth direction and a radius of action that decreases with depth. The formula is expressed as follows (Beentjes et al., 2019):

$$Q = \frac{9\eta U l e^3}{\pi (e^3 - 1)(h_e - h_i)(r_e^2 + r_e r_i + r_i^2)} \exp\left(\frac{-3r^2}{r_0^2}\right)$$
 (7)

$$r_0(z) = r_i + (r_e - r_i) \frac{h - h_i}{h_e - h_i}$$
 (8)

where Q is the bulk heat flow density, W/m^2 ; η is the thermal efficiency, dimensionless; U and I are the plasma current and voltage, respectively, V and V, respectively. V is a function of V and V, respectively.

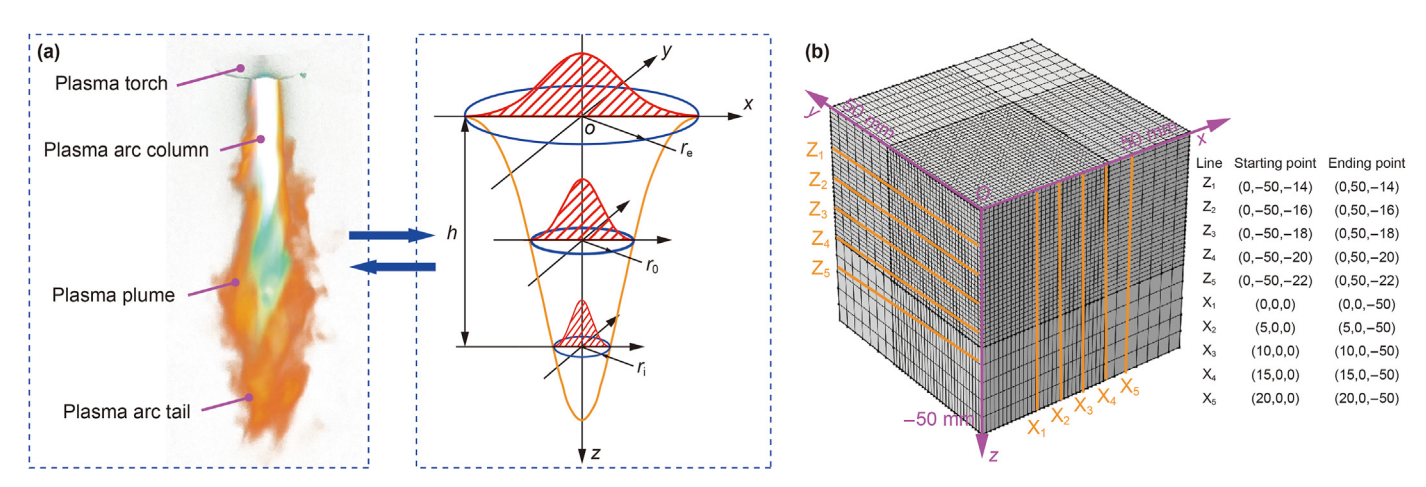


Fig. 7. Plasma jet photographs and heat source models (a) and quarter granite model (b).

heat distribution coefficient with respect to the depth h, $r_{\rm e}$ and $r_{\rm i}$ are the maximum and minimum radius with values of 18 and 13 mm, respectively. $h_{\rm e}$ and $h_{\rm i}$ are the maximum and minimum values in the z-direction at a depth h of 35 mm. The parameters are obtained through experimental data and iterative debugging of simulation. The heat source model is shown in Fig. 7(a). Researchers usually set the energy utilization rate of plasma arc between 0.5 and 0.8. This study sets η to 0.7 after comprehensive consideration (Duan et al., 2023; Yang et al., 2024).

At present, there is no engineering model for plasma drilling technology to refer to. Therefore, the following assumptions are given to simplify the model. (1) The target rock formation is granite, which is a homogeneous and isotropic material. (2) The effect of confining pressure on thermal melting of granite is ignored. (3) The chemical reactions during the melting process are ignored. Experimental observations reveal that the drilling depth achieved by the plasma jet within 30 s does not exceed 50 mm, thereby determining the model dimensions to be 100 mm \times 100 mm \times 50 mm. Fig. 7(b) displays a quarter section of the simulation model. The physical properties of the material used the tested results of the rock sample in Section 2.1, as shown in Table 1. Since the arc column primarily impacts the center of the granite surface, the mesh is refined in the area close to the z-axis. The total number of grid cells is 15360, and the average grid quality is 0.8588, which meets the calculation accuracy requirements. Heat conduction is mainly considered during the plasma action, and the "Solid Heat Transfer" module is used to realize transient heat transfer calculations in the model. The initial temperature of granite is 20 °C. Due to the poor thermal conductivity of granite, the bottom and sides are set as thermally insulating boundaries. The upper surface is the plasma jet action surface, and the boundary conditions are set to the heat source heat flux and phase change heat flux. The generation and change of granite holes are realized through the "Deformation Geometry" module, and the entire domain is set to "free deformation". Specify the normal grid movement speed of the upper surface as $v = Q/(\rho \cdot H_s)$, where H_s is the latent heat of phase change, kJ/kg.

3.2.2. Model validation

To validate the accuracy of the model, numerical simulations were compared with experimental results, as shown in Fig. 8. The rock samples with a plasma current of 200 and 300 A and rockbreaking time of 30 s were cut. Photographs showing both the top and cross-section views of samples were obtained. The comparison between the hole morphology and the contour plot from

numerical simulation shows a general agreement. However, the experimental hole size is larger than the numerical value. This is because while the granite undergoes thermal melting, the plume of the plasma jet induces spalling over a broader area of the granite. The experimental hole profile matches with the 557 °C isotherm in the simulation. Axially, the hole depth observed in the experiment is smaller than that predicted by the simulation. The anisotropy of granite significantly contributes to the difference between the simulation and the experiment, representing a challenge in accurately modeling the rock-breaking processes. Fig. 8(b) presents a comparative analysis of temperature data collected from the C1 hole thermocouples against simulation results under different plasma currents. The good agreement between numerical predictions and experimental data indicates the right selection of model parameters.

3.2.3. Analysis of granite temperature field simulation results

Fig. 9 shows the temperature distribution cloud plots of the upper surface and lateral cross-section of granite when the plasma current is 300 A and the rock breaking time is 5-30 s. Owing to temperatures higher than the melting temperature, the rock material inside the hole is removed in a molten manner, resulting in the creation of a bowl-shaped hole. The temperature distribution on the upper surface and cross-section of the rock shows symmetrical characteristics. It can be seen that the region exposed to the center of the plasma jet exhibits quite high temperatures, with peak temperatures occurring at the boundaries of the hot melt holes. Thermal diffusion and heat conduction within the granite is relatively slow, and the isothermal density around the holes is very high and the temperature gradient is large. The isotherms become sparser as the distance from the holes increased. The radius and depth of the melt hole increased with time. The expansion of molten hole leads to an expansion of the temperature rise-regions in the rock. In particular, the temperature and hole morphology of the rock changes significantly during the first 25 s, which indicates that the plasma jet has the most significant thermal removal effect on the rock at this stage.

Fig. 10 illustrates the variation of the internal temperature curves of the granite over time. The temperature along the radial coordinates on the upper surface of the granite for intervals of 2–30 s is presented in Fig. 10(a). The radial position of the peak temperature expands over time, indicating the increase of the molten hole. With increasing in time, the temperature profiles become steeper, reflecting an intensifying temperature gradient near the melt hole. Despite the enlargement of the melt hole, the

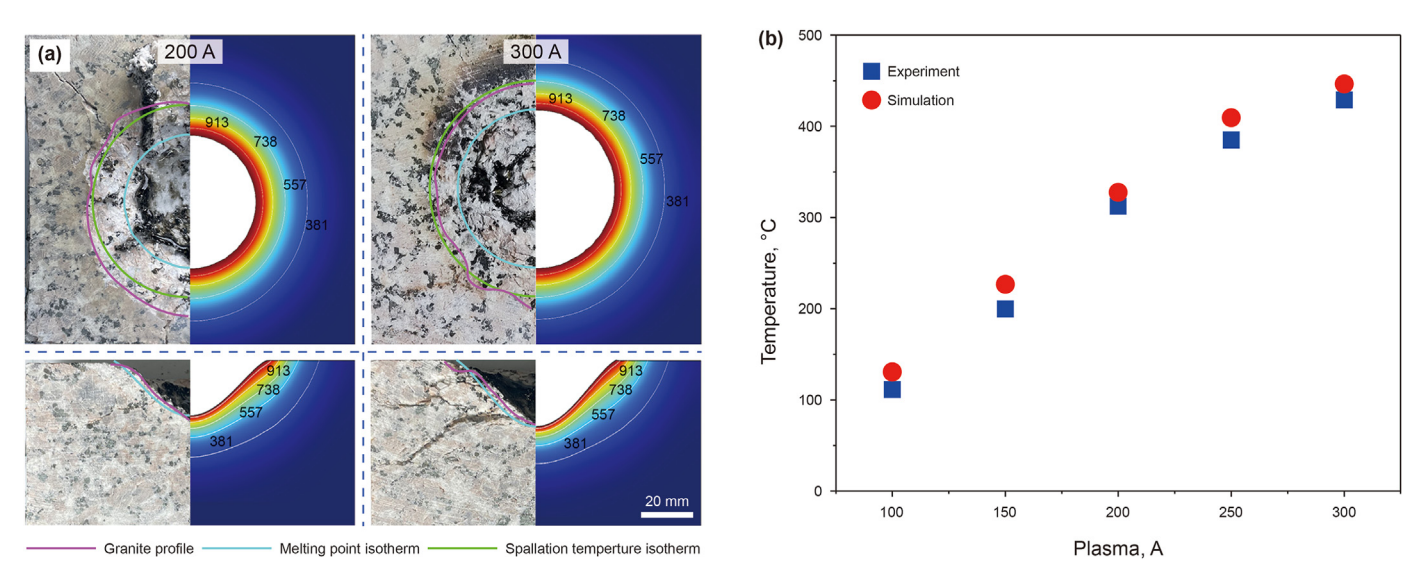


Fig. 8. Comparison of experimental and simulated results: (a) hole morphology, (b) temperature value.

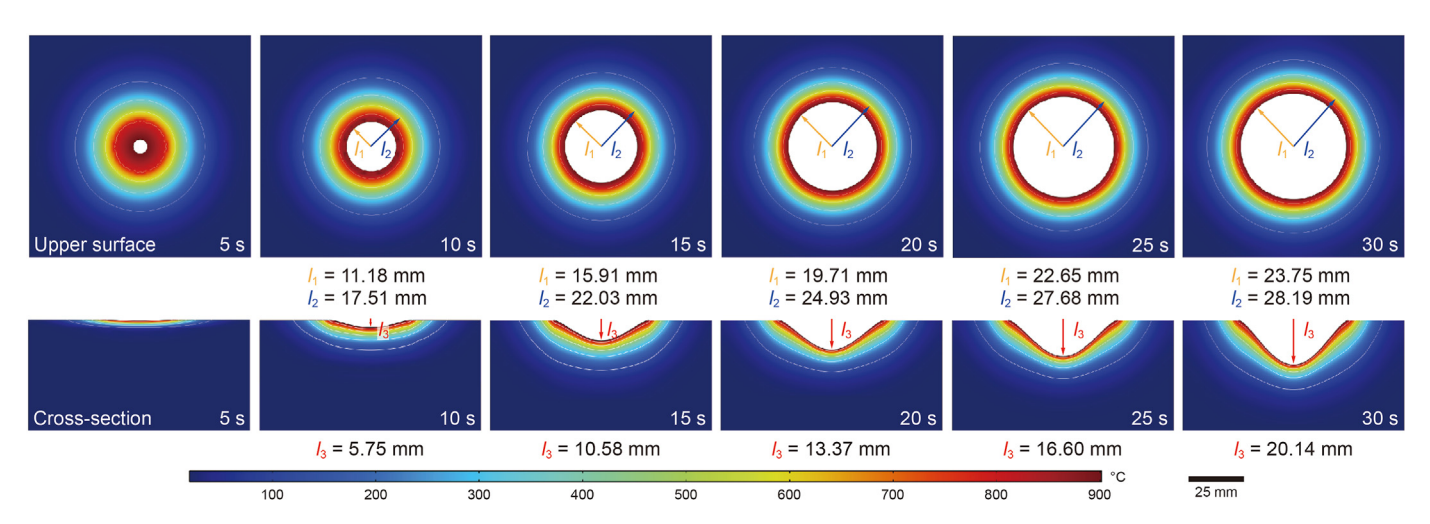


Fig. 9. Temperature distribution cloud plots of granite at different times.

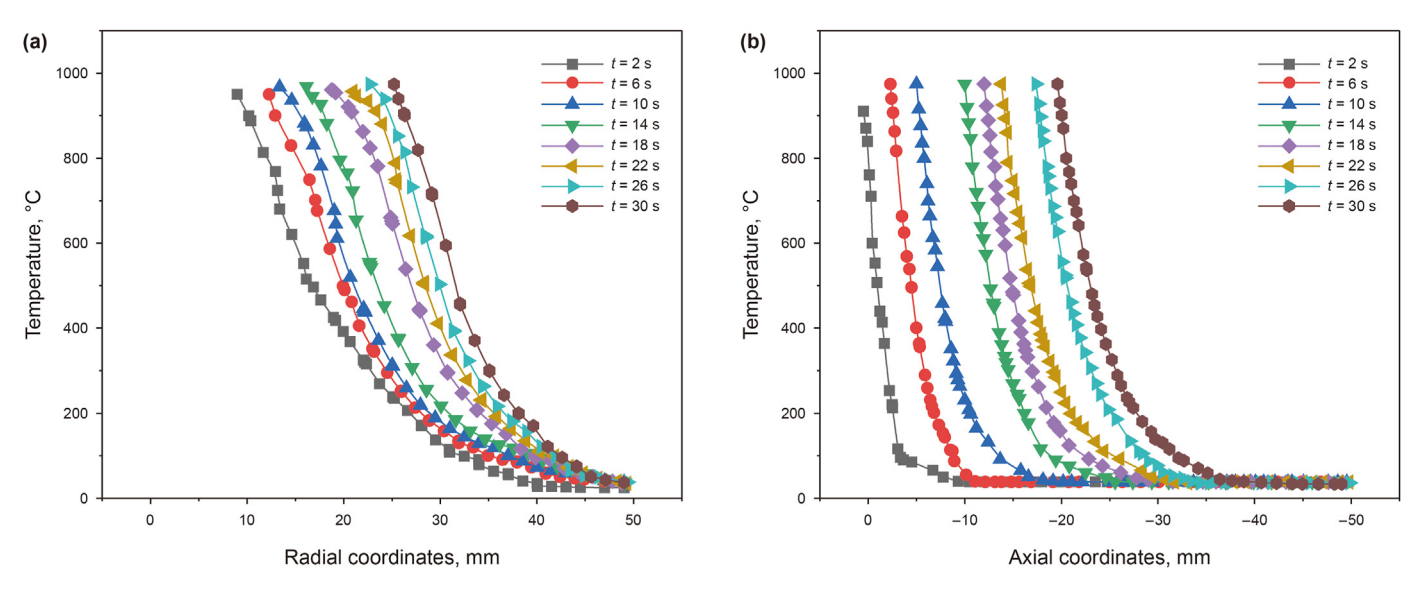


Fig. 10. Granite internal temperature field at different moments: (a) radial variation, (b) axial variation.

radial extent of thermal influence does not increase proportionally to the melt hole radius. In Fig. 10(b), the axial temperature change curve for long breakout times (such as t=30 s) slows down compared to that for short times (such as t=2 s). It suggests that in the later stages of rock-breaking, the axial thermal influence of the granite expands, and the axial temperature gradient decreases. It is consistent with the phenomenon observed in Fig. 9.

In this paper, the directional temperature distribution within the granite was investigated at time of 30 s and a plasma current of 300 A. Five temperature monitoring lines (X_1-X_5) were taken along the radial direction of plasma jet action and five monitoring lines (Z_1-Z_5) were also taken along the axial direction. The temperature monitoring lines positions and coordinates are shown in Fig. 7(b). The extracted temperature data curves are shown in Fig. 11. The radial temperature distribution patterns at different depths of the granite exhibit a consistent, with decreasing temperature with increasing radius, as illustrated in Fig. 11(a). The absence of data corresponds to the region of the molten hole. Temperatures are higher closer to the upper surface of the granite and decrease with depth at any given radius. As depth increases, the area experiencing a temperature rise shifts inward along the radius. It is attributed to the conical shapes of the holes, which are wider at the top and narrower at the bottom, causing the heat transfer area to align with the contours of the hole walls. When the depth is -22 mm, the granite is not perforated, so a complete temperature curve is presented. However, the temperature still reaches the maximum value at the center position. Fig. 11(b) shows the temperature distribution along the z-axis at varying radial positions. The axial temperature decreases with increasing radial coordinates. Locations closer to the radial origin experience a deeper penetration of the heating effect into the rock, resulting in higher temperatures at equivalent depths. This phenomenon is attributed to the Gaussian distribution of the energy of the plasma jet. At any given moment, areas closer to the radial origin receive more energy, leading to deeper penetration of heat into the rock via the hole walls. Consequently, as depicted in the figure, areas nearer to the radial center exhibit a steeper temperature gradient with depth, indicating a more pronounced axial temperature gradient.

Fig. 12 illustrates the internal temperature field of the granite subjected to plasma jet rock-breaking for 30 s under different plasma currents. Fig. 12(a) depicts the temperature along the radial direction on the upper surface of the granite. With an increase in

current, the heat-affected region expands, and the isotherm of melting temperature shifts outward from the center. The heating area inside the rock is distributed around the borehole wall, and the size and depth of the heating area become larger as the current increases. The temperature profiles of the rock along the z-axis under various currents are depicted in Fig. 12(b). The axial temperature distribution exhibits a consistent pattern at different currents. The peak temperature, corresponding to the molten point of the rock, is observed at the borehole wall, with a gradual decrease in temperature as the depth increases. As the current increases, the temperature at the same depth increases. It may be because that with increasing current, the diameter of the plasma arc column and the concurrent increase in energy density. Consequently, an augmented energy input at a constant rate accelerates the heating process of rock, resulting in a more pronounced temperature increase.

3.2.4. Effect of plasma jet rock-breaking at different initial temperatures

At present, the temperature of the developed HDR formations are usually in the range of 150–200 °C. In this section, the variation of rock-breaking effect of granite at initial temperatures of 150 and 200 °C is investigated. Fig. 13 shows the temperature cloud plots of two initial temperatures of granite under the action of plasma jet. The temperature distribution of granite with different initial values is consistent. The highest temperature occurs near the pit, and the heat-affected area is relatively limited. The higher the initial temperature, the sparser the isotherms near the pit. Fig. 14 shows the comparison of radius and removal volume of pits at different initial temperatures. In the early stage of rock-breaking (first 10 s), the values of hole radius and removal volume are larger and grow faster when the initial temperature is higher. Because the higher the initial temperature, the easier it is for granite to reach its melting point and undergo phase transition removal under the thermal shock of plasma jet. Moreover, whether after heat treatment or under real-time high temperature conditions, the internal cracks of granite further develop, leading to a weakening of the thermodynamic properties of the rock (Yin et al., 2016; Qin et al., 2020). Hightemperature granite is more likely to be removed under the instantaneous impact of plasma jet. After 10 s of rock-breaking, the values of hole radius and removal volume are almost equal for granites with different initial temperatures. This is because the

-50

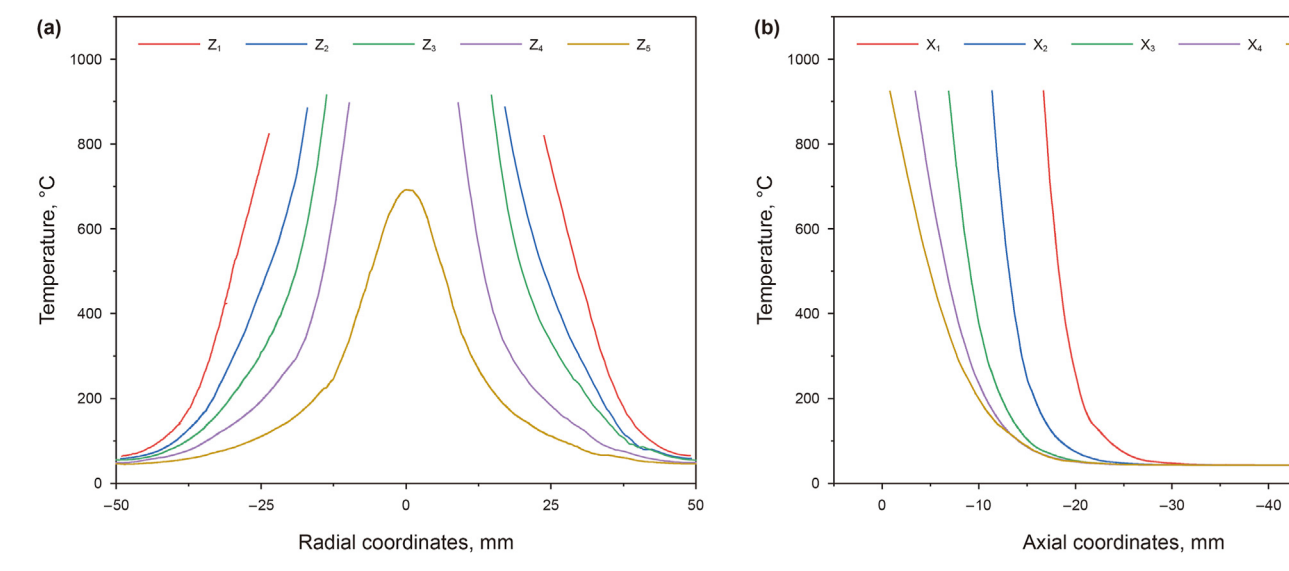


Fig. 11. Granite internal temperature at different monitoring lines: (a) axial variation, (b) redial variation.

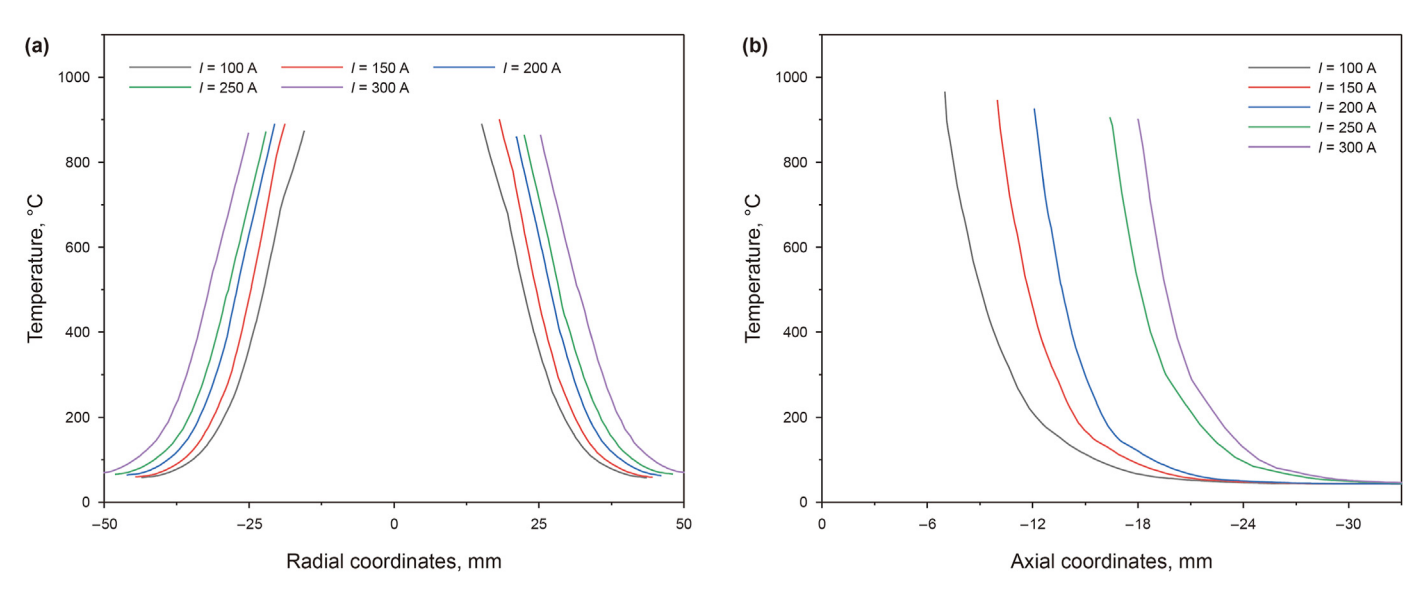


Fig. 12. Granite internal temperature field at different currents: (a) radial variation, (b) axial variation.

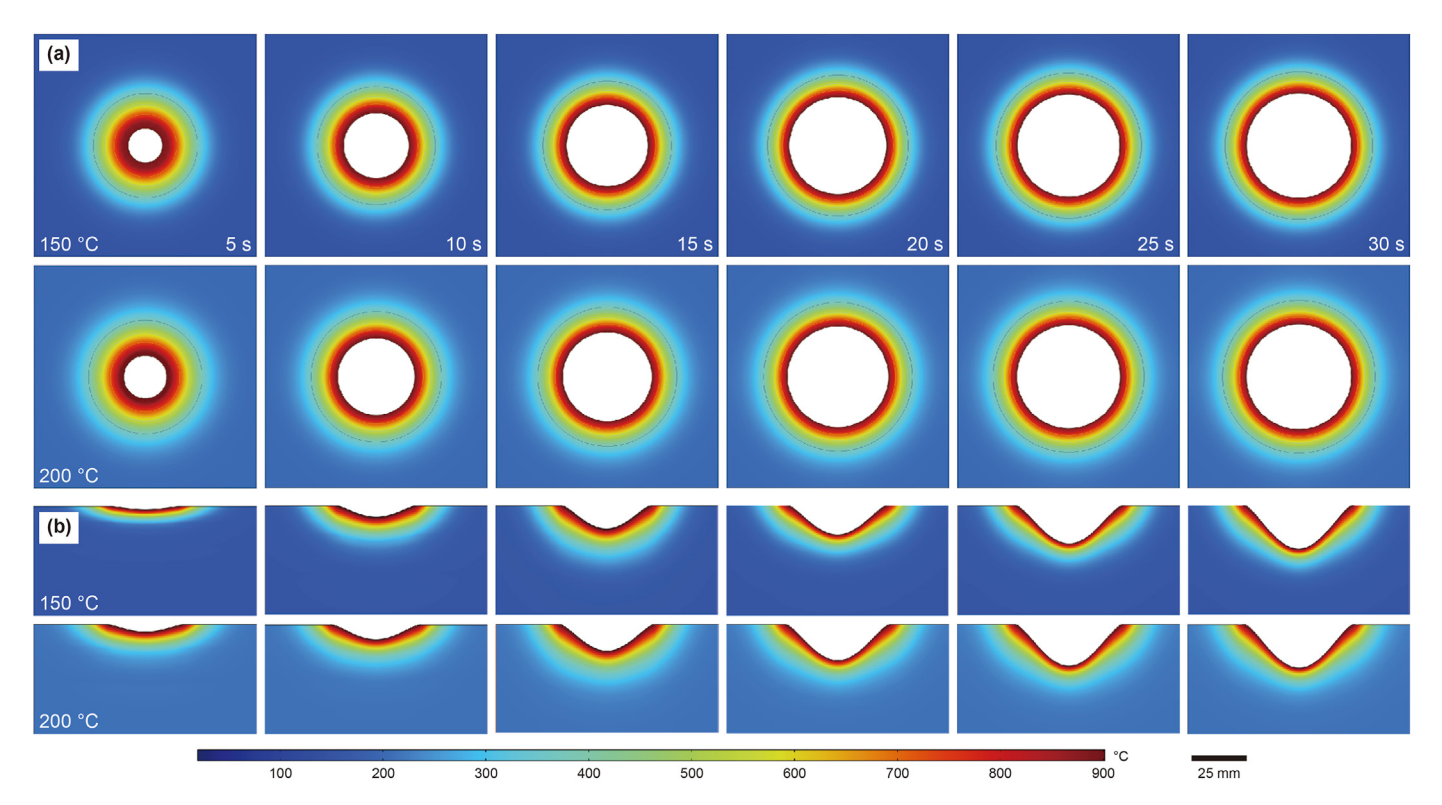


Fig. 13. Temperature cloud plots of granite at different initial temperatures: (a) upper surface and (b) cross-section.

thermal conductivity of granite is poor. Even though the initial temperature is high, the transfer of heat provided by the plasma jet inside the granite is limited in case the position of the plasma drill is fixed. The results and trends of melting removal by plasma jet are consistent for both room-temperature and high-temperature granite.

3.3. Analysis of the heat removal effect of plasma jet rock breaking

It is challenging to capture the granite removal effect at each instant during the rock-breaking process, however, it is readily

achievable through numerical simulations. Experiments are conducted for various rock-breaking durations (10, 15, 20, 25 and 30 s) utilizing a plasma current of 300 A. The radius of the granite hole observed in the experiments was compared with the radius of the spallation temperature isotherm and the radius of the melted holes derived from numerical simulations, as depicted in Fig. 15(a). During the initial stage of rock-breaking (t = 0 - 10 s), the radius of the granite aperture closely aligns with the radius of the spallation temperature isotherm. In middle stage (t = 10 - 20 s), the granite aperture remains close to the spallation temperature isotherm. The rate of increase in the radius of the melting point isotherm is similar

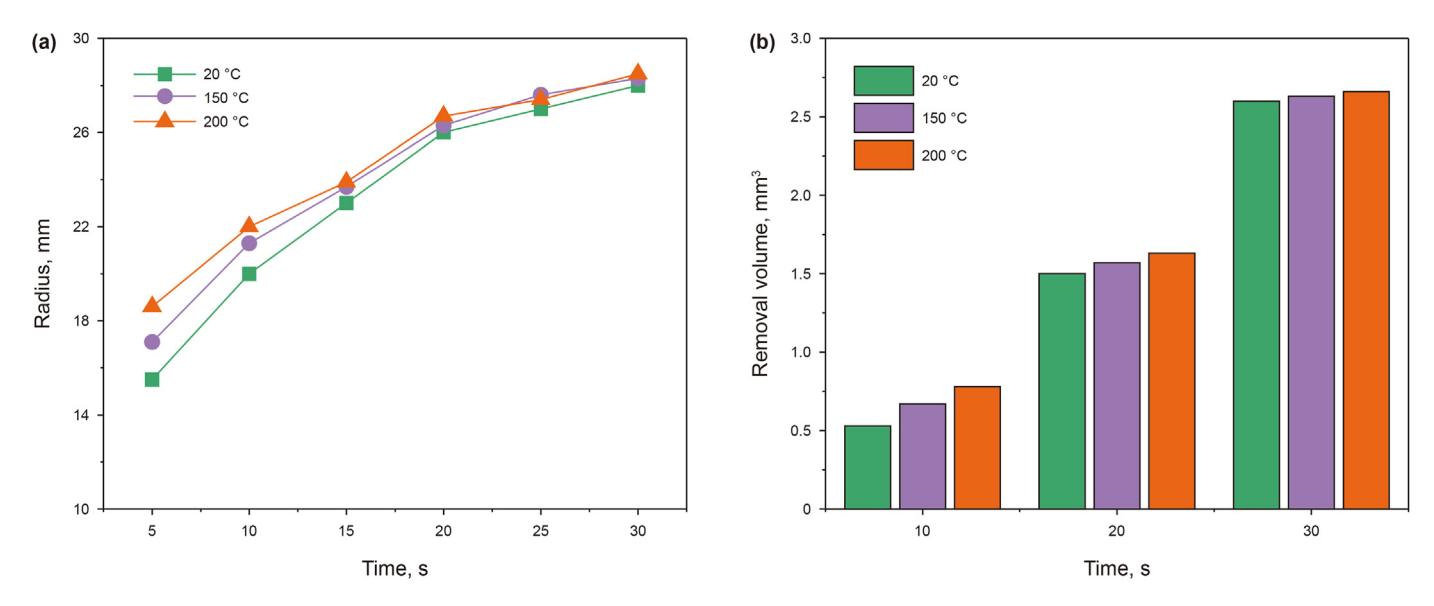


Fig. 14. Hole radius (a) and removal volume (b) at different initial temperatures.

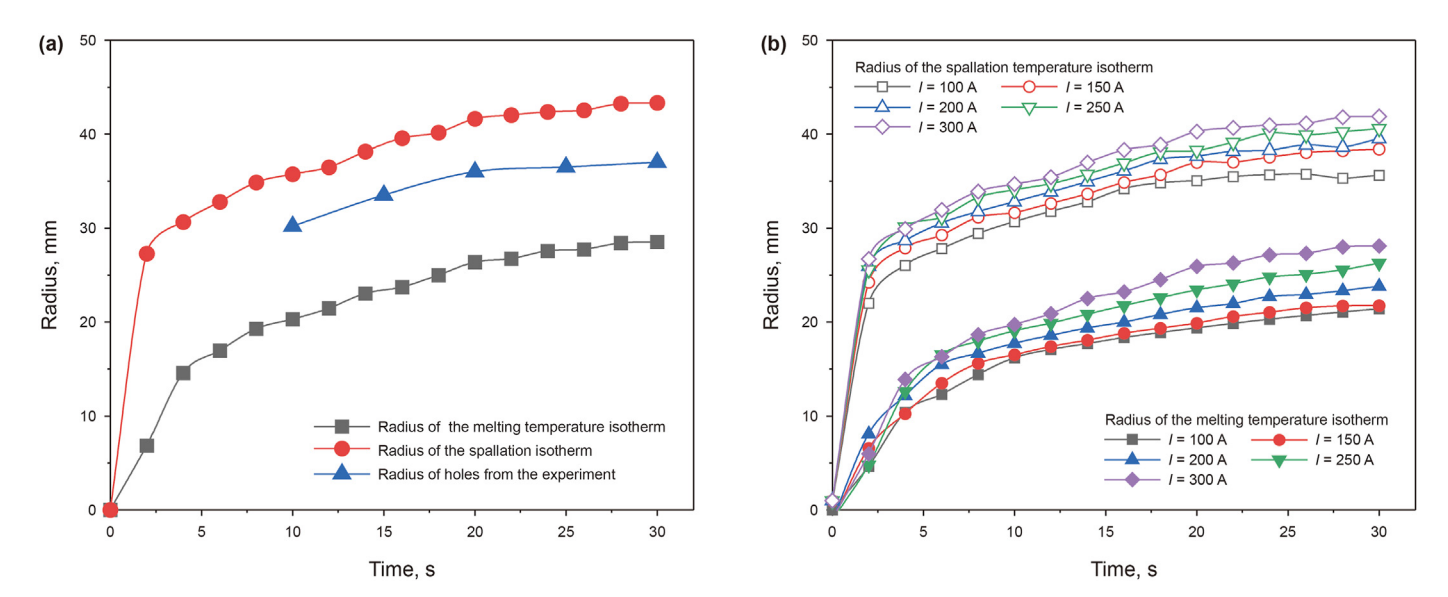


Fig. 15. Hole size variation: (a) comparison of experimental and simulated values, (b) simulated values at different currents.

to the rate of increase in the radius of the granite pore. After the rock-breaking time reaches 20 s, the growth rate of granite pore size and spalling temperature isotherm pore size slows down, but the radius of the melting point isotherm still maintains a relatively rapid growth rate. The radius of the melt hole begins to approach the radius of the granite. It can be predicted that if the rockbreaking time is extended, the melting point isotherm will be closer to the actual hole profile than the spallation temperature isotherm. Comparing the three curves suggests that within the initial 10 s of rock-breaking, the heat of the plasma jet instantaneously impacts the rock surface, elevating the temperature to the spalling threshold. Then, the rock begins to spall off and be removed in fragment. The heat conducted into the rock accumulates with time to reach the latent heat of melting of the granite. The thermal melting process proves to be significantly more efficient than thermal spallation, with the extent of thermal melting exceeding that of spallation. After the rock-breaking time reaches 20 s, the spread of the spalling temperature isotherm is nearly

stagnant due to the limitation of the radial influence range of the plasma jet heat source. Due to "overheating", the rock no longer breaks owing to different thermal expansion coefficients, and thermal melting becomes the dominant removal mechanism. Fig. 15(b) illustrates the variation of molten pore size and spallation temperature isotherms of granite over time under different plasma currents. During the middle to late phases of rock-breaking (t > 10 s), the expansion rate of the thermal melted hole radius markedly exceeds that of the spallation temperature isotherm. The plasma jet may provide sufficient energy to heat the granite surface of the holes to the melting point, resulting in initial melting. Nonetheless, the low specific heat capacity of granite significantly restricts the internal heat transfer. Despite continuous heat delivered from the plasma jet, the expansion of the heat-affected zone reaches a stable state.

A comprehensive examination of the plasma jet rock-breaking mechanism is essential for improving rock-breaking efficiency. Fig. 16(a) shows the comparison of the removal volume between

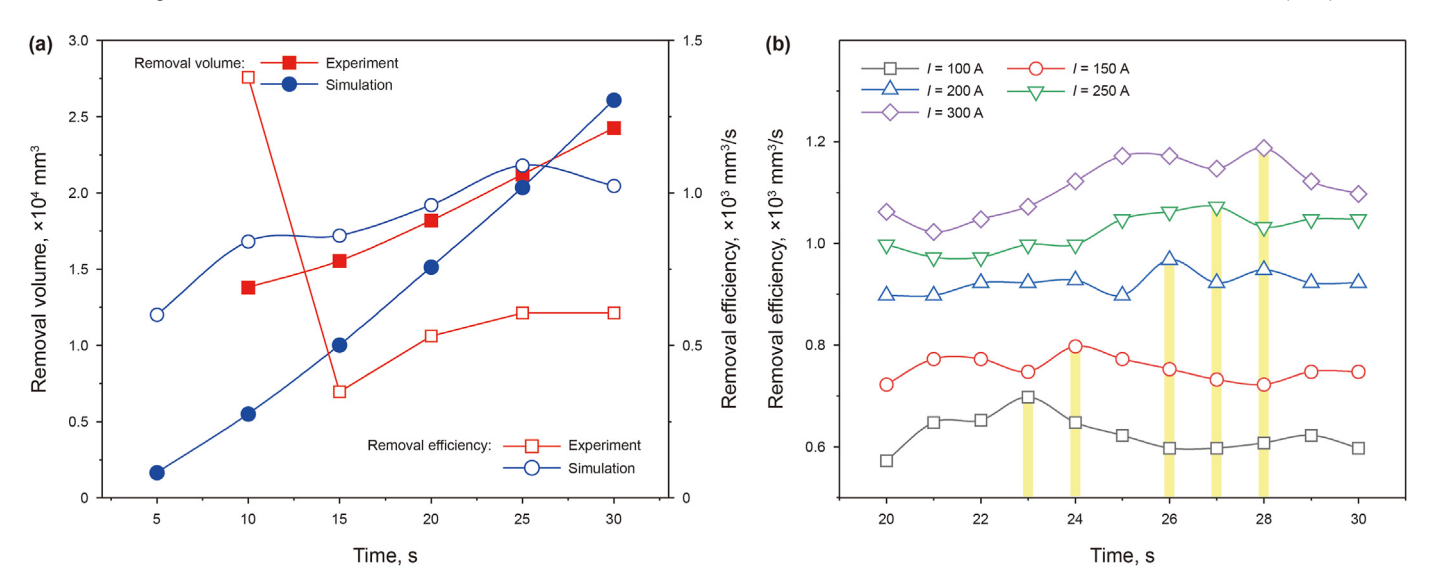


Fig. 16. Plasma jet rock-breaking effect: (a) comparison of experimental and simulated values, (b) removal efficiency of different currents in the late rock-breaking stage.

experiment and simulation. The removal efficiency is determined using the following equation:

$$\mu = \frac{V_i - V_{i-1}}{t_i - t_{i-1}}, (i = 1, 2, ..., 30)$$
(9)

where μ is the removal efficiency, mm³/s; V is the removal volume, mm³: t is the time. s.

Within the initial 25 s, the actual removal volume observed in the experiment exceeds that obtained from the simulation. This discrepancy is attributed to the jet impact on the granite, which induces a transient thermal shock, causing a pronounced contraction of thermal stresses within the rock mass. This initiates a rapid spalling phase, while the intense heat density simultaneously causes the rock to undergo a melting removal. Hence, due to the synergistic effects of both removal mechanisms, the volume of rock removed in the initial 25 s of rock-breaking surpasses the simulated value that only account for thermal melting. During the 25-30 s of rock breaking, spalling removal gradually stops, and the magma accumulated in the melt hole increases. The substantial distance between the plasma torch and the bottom of the pit make it difficult to expel all magma from the bottom of the pit. The molten magma continuously and repeatedly absorbs the heat energy of the iet, causing the experimental value to be lower than the simulated value under ideal conditions. Since the removal volume values in the first 10 s were not obtained experimentally, the removal efficiency value in the 10th s has no reference significance. The experimental values of removal efficiency follow the same trend as the simulated values after 15 s. Maximum removal efficiency occurs in the later stages of rock-breaking (20-30 s). Consequently, the removal efficiencies during the later stages of rock-breaking obtained through modeling are examined in detail in Fig. 16(b). The appearance of the maximum removal efficiency value is earlier with lower plasma currents because smaller plasma currents generate shorter plasma arcs, which in turn have a relatively limited axial reach on the rock. The plasma arc rapidly melts the granite to a certain depth, where the thermal melting capacity decreases, and similar to the removal efficiency. Overall, the plasma jet reached its maximum removal efficiency between 20 and 30 s of rock breaking. The drilling speed can be set accordingly to achieve higher breaking efficiency and lower energy consumption.

4. Discussion

High-energy plasma jets use high-temperature media to heat rock. The removal process is accompanied by a variety of complex phenomena, so it is crucial to study rock-breaking mechanisms in depth. Taking a plasma current of 300 A as an example, the mechanism of plasma jet rock breaking was analyzed and discussed based on the experimental phenomena and simulation results. Fig. 17(a) shows the schematic diagram of the different stages of the rock-breaking process, and Fig. 17(b) shows the photographs of the granite fragmentation morphology at the corresponding stages. In the first stage of rock-breaking, the damage area expands rapidly due to the instantaneous high-temperature impact of the plasma jet. The experimental data shows that the hole radius of 29.7 mm is close to the radius of the spallation temperature contour in the simulation of 30.19 mm. The temperature gradients in the radial and axial directions of the simulation reached 38.79 and 66.13 °C/ mm, respectively, and the huge temperature gradients caused the granite to undergo spalling. Then, in the second stage, the energy provided by the plasma arc reaches the latent heat of melting of the granite, and thermal melting of the rock begins to occur in the central region where the jet acts. Meanwhile, the upper surface of the granite continues to increase in the area where spallation occurs under the thermal influence of the plasma arc column. The thermal molten area grows rapidly and the radius expands by 7.89 mm, while the range of the spallation temperature isotherm slows down. At this stage, spallation removal is still the dominant method, thermal melting removal begins. Black particles formed by magma solidification appear in the granite holes. In the third stage of rock breaking, the area where the rock is melted is further expanded and the molten magma is discharged to the borehole wall by the strong airflow blowing action of the plasma jet. The exposed pit floor is removed continuously by the jet. At this time, in the radial direction, the heat-affected zone of the plasma arc column may have "overheated" the rock. The range of thermal spallation (radius of 40.61 mm) has no longer expanded, and the hole radius of the rock has reached 37.2 mm. This stage provides efficient removal of rock by thermal melting with removal efficiencies up to 1188 mm³/s. Ring-shaped black glassy material appears on the side wall of the granite hole, and macro cracks appears on the upper surface. As the drilling depth increases and enters the fourth stage, the distance between the bottom of the pit and the plasma torch is

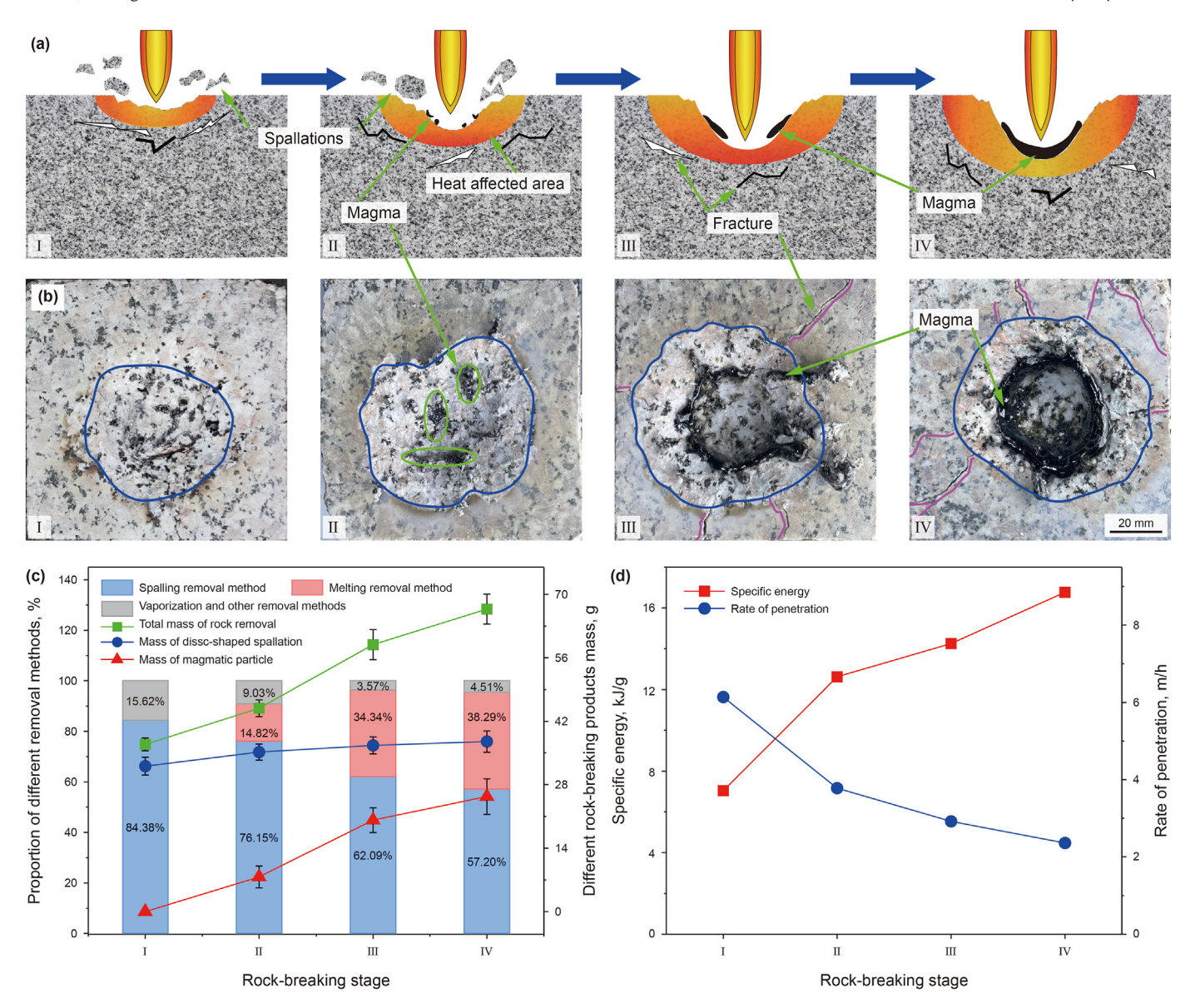


Fig. 17. Schematic diagram of mechanism (a), granite photograph (b), percentage and mass of different removal methods (c), and specific energy and rate of penetration (d).

so large that it is beyond the range of action of the arc column with its concentrated energy density. Only the arc tail with dispersed energy and insufficient "stiffness" remains in contact. Meanwhile, an increasing amount of melted magma in the hole gradually accumulates at the bottom of the pit, making it no longer possible to increase the depth. As shown in the photographs, the inside of the granite hole is completely covered with solidified magma and the number of cracks is rapidly increasing. The total mass of rock removed, the mass of rock fragments, and the mass of magma solidified material in the four stages were experimentally counted and analyzed as a percentage, as shown in Fig. 17(c). Consistent with the results of the above analysis, in Stage I, removal is carried out by spalling and no hot melting occurs. After entering Stage II, hot melting begins to occur, with a gradual increase in the percentage, and the mass of disc-shaped fragments tends to stabilize. The specific energy and rate of penetration of the plasma jet breaking rock are shown in Fig. 17(d). The SE of thermal spallation is the lowest in Stage I and increases after thermal melting occurs in Stages II and III. Since the position of the plasma drill bit is fixed in the experiment, the plasma jet cannot continue to break the rock when the granite hole reaches a certain depth. Thus, the *ROP* becomes a decreasing trend. In Stage IV, the *ROP* is lowest and the *SE* shows a steeper upward trend due to deeper hole depths and repeated melting of magma by the plasma jet.

The findings indicate that granite presents thermal spallation under the action of plasma jets with short duration and at low energies. Whereas granite will undergo high-temperature melting under the continuous action of the jet with high energy. The plasma jet expands the rock fragmentation area in the radial direction by thermal spallation and quickly and efficiently increases the hole depth in the axial direction by thermal melting using an arc column with substantial energy density (Duan et al., 2023; Wu et al., 2024). The significant radial temperature gradient of the plasma jet results in the formation of a heat-affected zone with a pronounced temperature gradient within the granite despite its low specific heat capacity. Consequently, the plasma jet rock-breaking method possesses the advantages of an extensive breaking area and a high breaking rate.

5. Conclusions

This study combines experimental and numerical simulations to investigate the thermal spalling and thermal melting processes of high-energy plasma jets breaking rock. The threshold temperature for granite spalling induced by plasma jet was deduced, the temperature rise characteristics and breaking performance of granite during the thermal melting process were simulated, and the rockbreaking mechanism of plasma jet was discussed. The following conclusions are drawn from the analysis and discussion of the results:

- (1) The average spalling temperature of plasma jet is 557 °C, and the spalling temperature shows an upward trend with the increase of plasma current. The temperature at which spallation occurs in the central area, where the plasma jet arc column acts, is lower than the area where the plasma plume acts. The threshold temperature of plasma jet-induced thermal spalling of granite is lower than that of the laser beam and flame jet reported in most studies.
- (2) Plasma jets can quickly heat the surface of granite, creating a huge thermal gradient within the rock. The temperature gradient along the axial direction of plasma jet action in granite is always greater than that in the radial direction. The temperature rise area inside granite expands with increasing plasma current and time. The plasma current is a key factor affecting the temperature field distribution inside granite.
- (3) The maximum removal efficiency of granite by plasma jet occurs between 20 and 30 s of rock-breaking time. When the plasma current is 100–300 A, the maximum removal efficiency is 697–1188 mm³/s.
- (4) Plasma jet rock breaking can be divided into three stages. In the first stage, the granite is removed by spalling, and the product is rock chips. The hole diameter expands rapidly. In the second stage, thermal melting begins, and the mass proportion of molten magma particles produced is 14.82%. In the third stage, thermal melting is the main removal method. The removal efficiency reaches the maximum, and many obvious macro cracks appear in the granite.

Future studies will investigate the thermal effects of plasma jets from a microscopic perspective, aiming to explore how various mineral compositions within rocks impact the spalling and thermal melting mechanism. Additionally, the impact of natural cracks on the heat transfer capabilities of plasma jets will be examined.

CRediT authorship contribution statement

Yan-Cong Han: Writing — review & editing, Writing — original draft, Project administration, Methodology, Investigation, Formal analysis, Conceptualization. **Chao Zheng:** Writing — review & editing, Supervision, Project administration, Funding acquisition. **Yong-Hong Liu:** Supervision, Resources, Project administration, Funding acquisition, Conceptualization. **Xin-Lei Wu:** Visualization, Software, Data curation. **Ren-Peng Bian:** Validation, Investigation, Data curation. **Peng Liu:** Writing — original draft, Visualization, Methodology.

Declaration of competing interest

The authors declare that they have no known competing financial interests or personal relationships that could have appeared to influence the work reported in this paper.

Acknowledgments

This work was supported by the Excellent Youth Science Fund Project (Overseas) of Shandong Province (No. 2024HWYQ-045), the Taishan Scholars Project of Shandong Province (No. tsqn202211085), the National Natural Science Foundation of China (No. 5240051775), the Equipment Pre-Research Collaborative Foundation for Innovation Team from Ministry of Education of the People's Republic of China (No. 8091B042209), the Postdoctoral Fellowship Program of CPSF (No. GZC20242009), and the Shandong Postdoctoral Innovation Project (No. SDCX-ZG-202400192).

References

- Aghahosseini, A., Breyer, C., 2020. From hot rock to useful energy: a global estimate of enhanced geothermal systems potential. Appl. Energy 279, 115769. https://doi.org/10.1016/j.apenergy.2020.115769.
- Bai, G.G., Sun, Q., Jia, H.L., Ge, Z.L., Tang, L.Y., Xue, S.Z., 2022. Mechanical responses of igneous rocks to microwave irradiation: a review. Acta Geophys. 70, 1183—1192. https://doi.org/10.1007/s11600-022-00789-5.
- Baruffati, P.P., Ngueguim, M.E., 2023. The evolution of hard rock drilling in Norway: how new technology solved an old challenge. In: SPE Middle East Oil and Gas Show and Conference. SPE-213654-MS. https://doi.org/10.2118/213654-MS.
- Bazargan, M., Gudmundsson, A., Meredith, P.I., 2017. Feasibility of using plasma assisted drilling in geothermal wells. In: 4th Sustainable Earth Sciences Conference and Exhibition. https://doi.org/10.3997/2214-4609.201702130.
- Beentjes, I., Bender, J.T., Tester, J.W., 2019. Dissolution and thermal spallation of barre granite using pure water hydrothermal. Jets. Rock Mech. Rock Eng. 52 (5), 1339–1352. https://doi.org/10.1007/s00603-018-1647-2.
- Dai, J.C., Tian, K.J., Xue, Z.G., Ren, S.H., Wang, T.Y., Li, J.B., Tian, S.C., 2014. CO2-enhanced radial borehole development of shale oil: production simulation and parameter analysis. Processes 12 (1), 116. https://doi.org/10.3390/pr12010116.
- Duan, X.M., Li, Q., Xie, W.R., Yang, X.D., 2023. Wire arc metal additive manufacturing using pulsed arc plasma (PAP-WAAM) for effective heat management. J. Mater. Process. Technol. 311, 117806. https://doi.org/10.1016/j.jmatprotec.2022.117806.
- Fang, T.C., Ren, F.S., Liu, H.X., Zhang, Y., Cheng, J.X., 2022. Progress and development of particle jet drilling speed-increasing technology and rock-breaking mechanism for deep well. J. Pet. Explor. Prod. Technol. 12, 1697–1708. https://doi.org/ 10.1007/s13202-021-01443-4.
- Gao, M.Z., Yang, B.G., Xie, J., Ye, S.Q., Liu, J.J., Liu, Y.T., Tang, R.F., Hao, H.C., Wang, X., Wen, X.Y., Zhou, X.M., 2022. The mechanism of microwave rock breaking and its potential application to rock-breaking technology in drilling. Petrol. Sci. 19 (3), 1110–1124. https://doi.org/10.1016/j.petsci.2021.12.031.
- Guo, C.G., Sun, Y., Yue, H.T., Li, Q., He, S.Z., Zhang, J.Z., Zhang, Y., 2022. Experimental research on laser thermal rock breaking and optimization of the process parameters. Int. J. Rock Mech. Min. 160, 105251. https://doi.org/10.1016/j.ijrmms.2022.105251.
- Han, Y.C., Zheng, C., Liu, Y.H., Xu, Y.F., Liu, P., Zhu, Y.J., Wu, X.L., 2024. Study on the rock-breaking characteristics of high-energy pulsed plasma jet for granite. Geo. Sci. Eng. 232, 212466. https://doi.org/10.1016/j.geoen.2023.212466.
- Jia, C.Z., Pang, X.Q., Song, Y., 2023. Whole petroleum system and ordered distribution pattern of conventional and unconventional oil and gas reservoirs. Petrol. Sci. 20 (1), 1–19. https://doi.org/10.1016/j.petsci.2022.12.012.
- Jing, S.L., Song, X.Z., Zhou, M.M., Xu, Z.M., Sun, Y., Xiao, Abdulla, A., Ergun, K., 2024. Experimental investigation of the annular cross-sectional distribution of cuttings bed with drillpipe rotation in horizontal wells. Powder Technol. 436, 119520. https://doi.org/10.1016/j.powtec.2024.119520.
- Kant, M.A., Rudolf, von, Rohr, P., 2016. Minimal required boundary conditions for the thermal spallation process of granitic rocks. Int. J. Rock Mech. Min. 84, 177–186. https://doi.org/10.1016/j.ijrmms.2015.12.009.
- Li, H.L., Zhou, L., Lu, Y.Y., Yan, F.Z., Zhou, J.K., Tang, J.R., 2020. Changes in pore structure of dry-hot rock with supercritical CO₂ treatment. Energy Fuels 34 (5), 6059–6068. https://doi.org/10.1021/acs.energyfuels.0c00250.
- Li, M.Y., Han, B., Zhang, S.Y., Song, L.X., He, Q.K., 2018. Numerical simulation and experimental investigation on fracture mechanism of granite by laser irradiation. Opt Laser. Technol. 106, 52–60. https://doi.org/10.1016/j.optlastec.2018.03.016.
- Li, M.K., Ni, H.J., Wang, R.H., Xiao, C.Y., 2017. Comparative simulation research on the stress characteristics of supercritical carbon dioxide jets, nitrogen jets and water jets. Eng. Appl. Comp. Fluid. 11 (1), 357–370. https://doi.org/10.1080/ 19942060.2017.1293565
- Liu, P., Liu, Y.H., Zhang, Y.Z., Wang, Q.X., Wu, X.L., Ma, C., Bian, R.P., Zhu, Y.J., 2023. Experimental study of underwater plasma arc penetration parameters for oil wellheads. Geoenergy Sci. Eng. 229, 212153. https://doi.org/10.1016/ j.geoen.2023.212153.
- Pink, A., Patterson, A., Thoresen, K.E., 2023. Building a system to solve the challenges of drilling hot hard rock for geothermal and oil and gas. In: SPE International Association of Drilling Contractors Drilling Conference Proceedings. SPE-212438-MS. https://doi.org/10.2118/212438-MS.
- Qin, Y., Tian, H., Xu, N.X., Chen, Y., 2020. Physical and mechanical properties of

granite after high-temperature treatment. Rock Mech. Rock Eng. 53, 305–322. https://doi.org/10.1007/s00603-019-01919-0.

- Rauenzahn, R.M., Tester, J.W., 1989. Rock failure mechanisms of flame-jet thermal spallation drilling-theory and experimental testing. Int. J. Rock Mech. Min. 26 (5), 381–399. https://doi.org/10.1016/0148-9062(89)90935-2.
- Rossi, E., Jamali, S., Schwarz, D., Saar, M.O., Rudolf von Rohr, P., 2020. Field test of a combined thermo-mechanical drilling technology. Mode II: flame-assisted rotary drilling. J. Pet. Sci. Eng. 190, 106880. https://doi.org/10.1016/ j.petrol.2019.106880.
- Rui, F., Zhao, G.F., 2021. Experimental and numerical investigation of laser-induced rock damage and the implications for laser-assisted rock cutting. Int. J. Rock Mech. Min. 139, 104653. https://doi.org/10.1016/j.ijrmms.2021.104653.
- Sambo, C., Liu, N., Shaibu, R., Ahmed, A.A., Hashish, R.G., 2023. A technical review of CO₂ for enhanced oil recovery in unconventional oil reservoirs. J. Pet. Sci. Eng. 221, 111185. https://doi.org/10.1016/j.petrol.2022.111185.
- Steen, W.M., Mazumder, J., 2010. Laser material processing. In: Laser Material Processing, fourth ed. Springer, London, pp. 1–558. https://doi.org/10.1007/978-1-84996-062-5
- Sun, Q., Liu, Y.H., Han, Y.C., Wu, X.L., Liu, P., Jin, H., 2020. A novel experimental method of investigating anode-arc-root behaviors in a DC non-transferred arc plasma torch. Plasma Sources Sci. Technol. 29, 025008. https://doi.org/10.1088/ 1361-6595/ab652e
- Sun, Q., Liu, Y.H., Shen, Z.P., Han, Y.C., Wang, Q.X., Liu, P., 2023. A combined thermal spallation and melting technology by plasma jet for deep and hard rock reservoirs. SPE J. 28 (1), 49–63. https://doi.org/10.2118/212263-PA
- ervoirs. SPE J. 28 (1), 49–63. https://doi.org/10.2118/212263-PA.
 Tester, J.W., Herzog, H.J., Chen, Z., Potter, R.M., Frank, M.G., 1994. Prospects for universal geothermal energy from heat mining. Sci. Global Secur. 5, 99–121. https://api.semanticscholar.org/CorpusID:55717435.
- Walsh, S.D.C., Lomov, I.N., 2013. Micromechanical modeling of thermal spallation in granitic rock. Int. J. Heat Mass Tran. 65, 366–373. https://doi.org/10.1016/ i.iiheatmasstransfer.2013.05.043.
- Wang, F., Meng, D.H., Hu, K., Du, X., Pang, R., Zou, Y.L., Dong, W.G., He, B.G., 2024a. Thermo-mechanical coupling characteristics of granite under triaxial pressures and ultrahigh heating rates. Comput. Geotech. 167, 106098. https://doi.org/

- 10.1016/j.compgeo.2024.106098.
- Wang, H.J., Liao, H.L., Wei, J., Liu, J.S., Niu, W.L., Liu, Y.W., Guan, Z.C., Sellami, H., Latham, J.P., 2023. Stress release mechanism of deep bottom hole rock by ultra-high-pressure water jet slotting. Petrol. Sci. 20 (3), 1828–1842. https://doi.org/10.1016/j.petsci.2022.12.002.
- Wang, K.X., Liu, Z.B., Wu, M., Wang, C., Shen, W.Q., Shao, J.F., 2024b. Experimental study of mechanical properties of hot dry granite under thermal-mechanical couplings. Geothermics 119, 102974. https://doi.org/10.1016/j.geothermics.2024.102974.
- Wei, W.W., Shao, Z.S., Zhang, Y.Y., Qiao, R.J., Gao, J.P., 2019. Fundamentals and applications of microwave energy in rock and concrete processing a review. Appl. Therm. Eng. 157, 113751. https://doi.org/10.1016/j.applthermaleng.2019.113751.
- Weibull, W., 1951. A statistical distribution function of wide applicability. J. Appl. Mech. 18 (3), 293–297. https://api.semanticscholar.org/CorpusID:9800843.
- Wilkinson, M.A., 1989. Computational Modeling of the Gas-phase Transport Phenomena and Experimental Investigation of Surface Temperatures during Flame-Jet Thermal Spallation Drilling. Ph.D Thesis. Massachusetts Institute of Technology, Dept. of Chemical Engineering, pp. 135–142.
- Wilkinson, M.A., Tester, J.W., 1993. Experimental measurement of surface temperatures during flame-jet induced thermal spallation. Rock Mech. Rock Eng. 26 (1), 29–62. https://doi.org/10.1007/BF01019868.
- (1), 29–62. https://doi.org/10.1007/BF01019868.

 Wu, G.Y., Yu, D.P., Zhang, B., Peng, K.M., Islam, S., 2024. Arc column oscillation: a new mode of arc fluctuation in laminar plasma torch. Plasma Chem. Plasma Process. 44 (1), 115–130. https://doi.org/10.1007/s11090-023-10393-0.
- Yang, F.L., Liu, W.J., Zhu, X.H., Xiang, C., 2024. The rock-breaking mechanism of thermal spalling-assisted rock cutting by PDC cutter. Rock Mech. Rock Eng. 57 (2), 993–1012. https://doi.org/10.1007/s00603-023-03603-w.
- Yin, T.B., Shu, R.H., Li, X.B., Wang, P., Liu, X.L., 2016. Comparison of mechanical properties in high temperature and thermal treatment granite. T. Nonferr. Metal. Soc. 26 (7), 1926–1937. https://doi.org/10.1016/S1003-6326(16)64311-X.
- Zhu, Z.N., Yang, S.Q., Ranjith, P.G., Tian, W.L., Tian, H., Zheng, J., Jian, G.S., Dou, B., 2023. A comprehensive review on mechanical responses of granite in enhanced geothermal systems (EGSs). J. Clean. Prod. 383, 135378. https://doi.org/10.1016/j.jclepro.2022.135378.